Paper 98

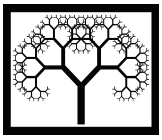

Proceedings of the Sixth International Conference
on Engineering Computational Technology,
M. Papadrakakis and B.H.V. Topping, (Editors),
Civil-Comp Press, Stirlingshire, Scotland

Viscoelastic Low-Reynolds-Number Flows in Mixing-Separating Cells

A. Afonso[1], M.A. Alves[1], R.J. Poole[2], P.J. Oliveira[3] and F.T. Pinho[1,4]
[1] Chemical Engineering Department, CEFT, Faculty of Engineering
University of Porto, Portugal
[2] Department of Engineering, University of Liverpool, United Kingdom
[3] Department of Electromechanics Engineering, MTP Unit
University of Beira Interior, Covilhã, Portugal
[4] University of Minho, Braga, Portugal

Abstract

In this work we investigate the flow of Newtonian and viscoelastic fluids in a mixing-separating geometry consisting of two opposed channel flows interacting through a gap in the common separating wall. This type of flow was experimentally investigated by Cochrane et al. [1] using Newtonian and viscoelastic fluids at low Reynolds number flows ($Re < 40$). In the present numerical study we assess the effects of Deborah and Reynolds numbers and gap size on the two-dimensional flow dynamics. The normalized gap size was varied between 0 and 5, *Re* varied between 0 and 50 and *De* varied between 0 and the maximum attainable value.
For Newtonian fluids the creeping flow is anti-symmetric, due to the anti-symmetry of the fully-developed inlet conditions and the symmetry of the flow geometry. Increasing the gap size increased the reversed flow rate ratio (R_r), here defined as the ratio between the reversed and total flow rates. In this investigation we also investigate in detail the creeping flow of viscoelastic fluids obeying the upper-convected Maxwell model for which two distinct flow patterns are found. For normalized gap sizes below a critical value the reversed flow is slightly enhanced by viscoelasticity, followed by a decrease in R_r towards zero as *De* further increases. For a supercritical gap size viscoelasticity is responsible for a continuous increase in R_r. This flow type transition can be exploited to promote mixing, and this application will also be addressed in this work.

Keywords: mixing-separating, low Reynolds number, viscoelastic fluids, UCM model, elastic instabilities, flow bifurcation.

1 Introduction

A simple constitutive model, the upper-convected Maxwell (UCM) model, is used to simulate viscoelastic flows in a mixing and separating geometry [1]. This flow has been previously investigated experimentally and numerically by Cochrane et al. [1],

Walters and Webster [2] and in purely numerical studies by Baloch et al. [3] and Fiétier [4]. In their numerical contribution Cochrane et al. [1] used a finite-difference discretization with the UCM model to represent the behavior of a highly-elastic constant-viscosity "Boger" fluid [5]. They investigated the effects of gap width (g) for two different flow configurations: one with equal flow rates in the two inlet channel arms and the other with unbalanced flow rates. In a sequel paper [2], consideration was given to flows using thin insert plates with rounded edges. In both experimental works, this complex flow displayed remarkable flow features and distinct Newtonian and elastic-flow behaviors, with the presence of unidirectional and reversed flows in varying degrees. Later, Baloch et al. [3] used the Phan-Thien−Tanner (PTT) model [6] to simulate this flow also using thin insert plates with rounded edges and equal flow rates at the inlet channels. Fiétier [4] used a spectral element method to simulate the flow of a FENE-P model [7] for the case with a thick insert plate with rounded edges. He was able to capture qualitatively the experimental results of [2].

In this work we extend the limited information on the variety of viscoelastic fluid flow behavior in the mixing and separating geometry, clarifying and mapping flow configurations for different gap sizes under conditions of low inertia and high viscoelasticity. We also attempt to assess the existence and extent of purely-elastic flow instabilities. These types of instability are present in extension-dominated flows, in particular in flows containing a stagnation point, such as the cross-slot [8-10], and the viscoelastic opposed jet [11]. Poole et al. [9] simulated the two-dimensional cross-slot flow of an UCM fluid under creeping-flow conditions, and were able to capture qualitatively the onset of a bi-stable steady asymmetric flow, above a first critical Deborah number, followed by a later transition to a time dependent flow. These numerical results were in qualitative agreement with the experimental findings of Arratia et al. [7]. Poole et al. [10] incorporated the effect of solvent viscosity, leading to the Oldroyd-B constitutive equation, and finite extensibility (using the PTT model), and proposed β-*Re-De* and ε-*Re-De* maps delimiting different flow pattern types. These maps showed the existence of a narrow region of steady asymmetric flow in the β-ε-*Re-De* space and identified the limiting *De* for onset of time-dependent flow.

In this work we focus on the mixing-separating flow geometry with zero thickness insert plates and equal flow rates at the two channel inlets.

2 Governing equations and numerical method

The equations we need to solve are those of conservation of mass

$$\nabla \cdot \mathbf{u} = 0 \tag{1}$$

and momentum

$$\rho \frac{\partial \mathbf{u}}{\partial t} + \rho \nabla \cdot \mathbf{u}\mathbf{u} = -\nabla p + \nabla \cdot \boldsymbol{\tau} \tag{2}$$

coupled with an appropriate constitutive equation for the extra stress, $\boldsymbol{\tau}$. Here, for reasons of rheological simplicity, we use the UCM model,

$$\boldsymbol{\tau} + \lambda\left(\frac{\partial \boldsymbol{\tau}}{\partial t} + \mathbf{u}\nabla\cdot\boldsymbol{\tau}\right) = \eta\left(\nabla\mathbf{u} + \nabla\mathbf{u}^{\mathrm{T}}\right) + \lambda\left(\boldsymbol{\tau}\cdot\nabla\mathbf{u} + \nabla\mathbf{u}^{\mathrm{T}}\cdot\boldsymbol{\tau}\right) \tag{3}$$

where λ and η are the relaxation time and shear viscosity of the fluid, respectively. A fully-implicit finite-volume method was used to solve Equations (1) – (3). The method is based on a time marching pressure-correction algorithm formulated with the collocated variable arrangement and is explained in detail in Oliveira et al. [12] and Alves et al. [13]. Briefly, the governing equations are transformed first to a non-orthogonal coordinate system, but retaining the Cartesian velocity and stress components. This approach is advantageous from a numerical point of view because the equations are written in a strong conservative form, which helps to ensure the conservation of physical quantities through the conservativeness of the final algebraic equations. Then, the equations are integrated in space over the control volumes (cells with volume V_{P}) forming the computational mesh, and in time over a time step (δt), so that sets of linearised algebraic equations are obtained, having the general form:

$$a_{\mathrm{P}}u_{\mathrm{P}} = \sum_{\mathrm{F}=1}^{6} a_{\mathrm{F}}u_{\mathrm{F}} + S_U \tag{4}$$

to be solved for the velocity components, and

$$a_{\mathrm{P}}^{\tau}\tau_{\mathrm{P}} = \sum_{\mathrm{F}=1}^{6} a_{\mathrm{F}}^{\tau}\tau_{\mathrm{F}} + S_{\tau} \tag{5}$$

to be solved for the polymeric contribution to the extra stress components, τ_{ij}. In these equations a_{F} are coefficients accounting for convection and diffusion, S are source terms encompassing all contributions that are not included in the terms with coefficients, the subscript P denotes the cell under consideration and subscript F its corresponding neighbouring cells. The central coefficient of the momentum equation, a_{P}, is given by

$$a_{\mathrm{P}} = \frac{\rho V_{\mathrm{P}}}{\delta t} + \sum_{\mathrm{F}=1}^{6} a_{\mathrm{F}} \tag{6}$$

After assembling all coefficients and source terms, the linear sets of equations (4) are solved sequentially for the Cartesian velocity components. These newly-computed velocity components do not, in general, satisfy the continuity equation and need to be corrected by an adjustment of the pressure differences which drive them. This adjustment is accomplished by means of a pressure-correction field

obtained from a Poisson pressure equation according to the SIMPLEC algorithm [14]. Once a velocity field satisfying continuity has been obtained, the implicitly-discretized constitutive equations for the polymeric contribution to the extra stress components (i.e. Eq. 5) are solved sequentially. To formulate the convective fluxes, the code uses the CUBISTA high-resolution scheme, especially designed for differential rheological constitutive relations [13].
Along with inertial effects, in this work we will also focus on creeping-flow conditions, in which case the advective term in the momentum equation is neglected.

3 Geometry and computational meshes

The flow domain and problem is that of two opposed channel flows interacting through a gap of nondimensional width ($\theta = g/H$) in the middle of the thin separating wall of thickness a (defining the nondimensional thickness $\alpha = a/H$), as shown schematically in Figure 1. The two inlet channels have the same width (H) and lengths $L = 20\,H$.

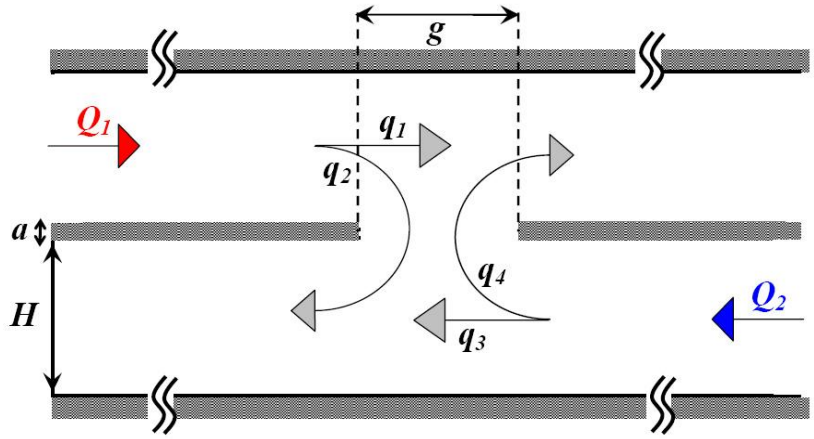

Figure 1: Diagram of the mixing-and-separating flow geometry.

At the inlets fully-developed velocity and stress profiles are imposed and the inlet length is more than sufficient for the flow in the central region to be independent of the inlet condition. No-slip conditions are imposed at all channel walls and at the outlet planes Neumann boundary conditions are applied to all variables including the pressure gradient, i.e. $\partial\varphi/\partial x = 0$.
For all θ values the computational domain was mapped using six blocks, one in each channel and two in the central region. The main characteristics of the two meshes used in this work for $\theta = 1$ are given in Table I, including the total number cells (NC), the number of control volumes in the central region in both x and y directions (NCS), and the minimum cell spacing which occurs also in this central region (Δx_{min} and Δy_{min}). For other plate thicknesses the meshes were adapted to have the same characteristics.
For each value of θ different meshes were used with different number of cells in the x and y directions, but always ensuring consistent mesh refinement and that the minimum cell spacing in both directions remained essentially the same (i.e. square

control volumes). As a consequence, for all meshes used, in the central region the cell spacing was uniform and progressively refined from $\Delta x_{min} = \Delta y_{min} \approx 0.04H$ for mesh M25L to $\Delta x_{min} = \Delta y_{min} \approx 0.02H$ for mesh M51L. These two-dimensional meshes contain 25 704 and 35 904 cells corresponding to about 179 928 and 251 328 degrees-of-freedom (DOF), for low and large adimensional gap width, respectively.

	NC	DOF	NCS_X	NCS_Y	$\Delta x_{min}/H$	$\Delta y_{min}/H$
M25L (θ=1)	6 300	44 100	26	25	0.0385	0.04
M51L (θ=1)	25 704	179 928	52	51	0.0186	0.0196

Table 1: Main characteristics of the computational meshes ($\theta = 1$).

The results presented in the next section are in dimensionless form, unless otherwise stated. Velocities are normalised by the bulk velocity in the inlet channels (U) and the stresses are normalised by $\eta U/H$. The Deborah number is the ratio between the fluid relaxation time (λ) and a flow time scale, here taken as g/U, i.e., $De = \lambda U/g$. For flows with inertia the Reynolds number is defined as $Re = \rho UH/\eta$. To quantify the degree of flow reversal relative to unidirectional flow existing in the absence of a gap in the middle wall, the parameter $R_r = q_2/Q_1 = q_4/Q_2$ is used, where q_2 and q_4 correspond to the partial flow rates that reverse from each inlet arm and $Q_1 = Q_2$ are the total flow rates at each inlet channel, as illustrated in Figure 1.

4 Results and discussion

4.1 Calculation accuracy

In this section we assess the convergence with mesh refinement in order to provide a measurement of the numerical uncertainty. Figure 2 plots the predicted transverse profiles of the normalised velocity and first normal-stress difference at $x/H = 0$, i.e., in the stagnation point at the middle of the gap. The data from the two meshes pertain to the flow of an UCM fluid at $De = 0.35$, $Re = 0$, $\theta = \sqrt{2}$ and $\alpha = 0$, which corresponds to a sub-critical flow gap condition. The velocity profiles from both meshes are almost undistinguishable from each other and exhibit excellent agreement. The stress profiles show a slight mesh dependency near the stagnation point due to the high stress gradients developing in that region, but elsewhere the agreement between both meshes is very good. In the remaining of the paper, unless otherwise stated, the results presented were obtained with mesh M51L.

4.2 Newtonian results

From a purely geometric point of view the mixing-and-separating geometry can be idealized as a cross-slot [9] with one pair of aligned arms rotated by 90° towards the other pair, leading to a nondimensional gap size of $\theta = \sqrt{2}$ and a vanishing separation plate thickness ($\alpha \to 0$). Had the flow type been maintained in this

operation, the ratio between the reversed to unidirectional flow would have been $R_r = 0.5$ to keep full similarity with the cross-slot, i.e, the flow that would be reversing and mixing in both the upper and lower exit sections would be identical as in the cross-slot geometry [9]. Obviously this is not the case as is well shown in Figure 3, where R_r is plotted as a function of normalised gap width, θ, for various plate thicknesses, α, for Newtonian inertialess flow. However, the difference is not that large because $R_r = 0.5$ for $\theta \approx 1.75$ or equivalently when $\theta = \sqrt{2}$ the degree of reverse to unidirectional flow is $R_r = 0.29$ ($\neq 0.5$). Figure 3 also shows that the effect of plate thickness for thin plates is small as found experimentally [1,2]. Figure 3 highlights the transition from a straight unperturbed no-reverse-flow situation at low θ to a full flow reversal when the gap is large.

The differences between the results for the cross-slot and the separating-mixing geometries may be understood from the different angles of the approaching flows near the stagnation points. In the present geometry these approach flows are not aligned with the channels and are not orthogonal as in the cross-slot flow. As a consequence in the present geometry shear flow plays a role in the stagnation point region which was absent from the cross-slot flow geometry which is purely extensional in character. This difference may also be important for understanding the appearance of the purely-elastic instabilities in the cross-slot geometry. These comments are better understood from inspection of Figure 4, where streamlines for the inertialess flow of Newtonian fluids at low, medium and large gap widths ($\theta = 1$, 2 and 2.83) are shown corresponding to $\alpha = 0$. These patterns correspond to the line for $\alpha = 0$ in Figure 3.

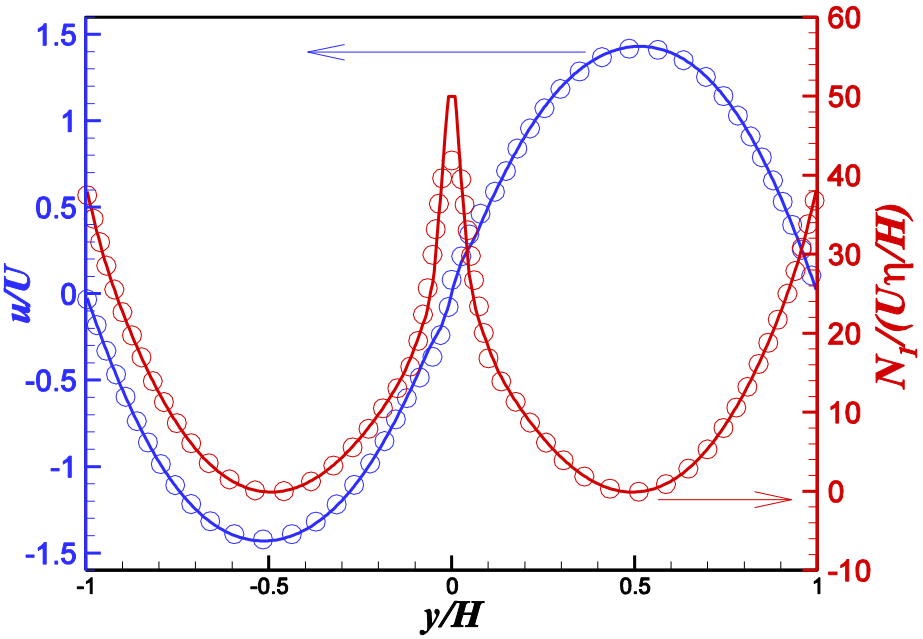

Figure 2: Transverse profiles of the normalised velocity and first normal stress differences at $x/H = -2$, for $De = 0.3$ ($Re = 0$, $\theta = 1.74$ and $\alpha \to 0$).

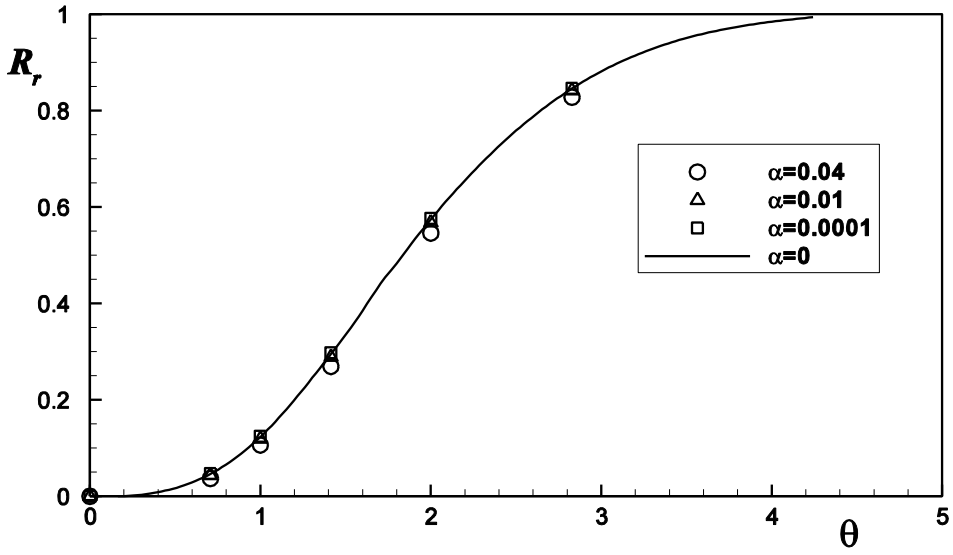

Figure 3: Degree of reverse to unidirectional flow for several gap widths, θ, and plate thickness, α, for the Newtonian case at Re=0.

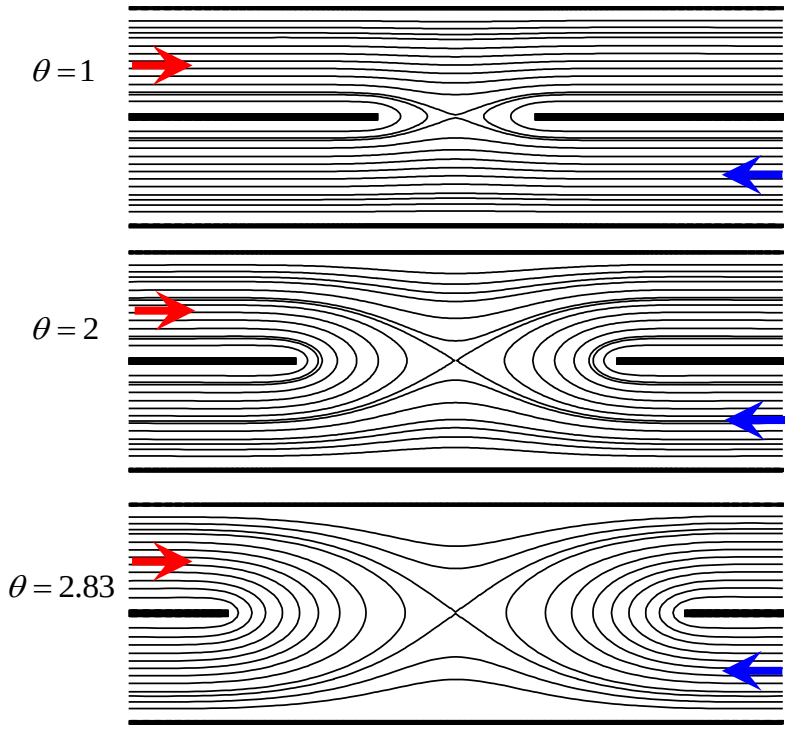

Figure 4: Streamlines for the mixing-and-separating geometry for several gap widths, θ, with α = 0, for the Newtonian case at Re = 0 using mesh M51.

The influence of flow inertia on R_r for Newtonian fluids is presented in Figure 5 as a function of the normalized gap width, θ□ . Regardless of the Reynolds number, R_r varies from 0 to 1 in the evolution from a small to a large gap in agreement with experiments [1,2]. For $Re \leq 1$ the variation of R_r with θ is independent of Reynolds number, but at higher Re inertia enhances flow reversal and this is observed to take

place for $Re = 10$ at $\theta \geq 1.7$ and for $Re = 50$ at $\theta \geq 1.2$ respectively. At some representative Reynolds numbers data from both meshes (M25L and M51L) are plotted in Figure 5. The good agreement confirms again that the use of mesh M51L is adequate for accurate predictions.

4.4 Viscoelastic/Inertial effects:

The creeping flow of UCM fluids exhibits an interesting bifurcation pattern, which depends on the gap width, as illustrated in Figure 6. For high non-dimensional gap sizes, but below a critical value ($\theta \leq 1.7$), the reversed flow is initially slightly enhanced by viscoelasticity, followed by a strong decrease in R_r towards zero as De further increases. This flow behavior is characterized by a significant deviation from streamline parallelism in the gap region although with the fluid still tending to flow unidirectionally as reported in previous experiments [1,2]. This is typified by the flow pattern shown in Figure 7 (a).

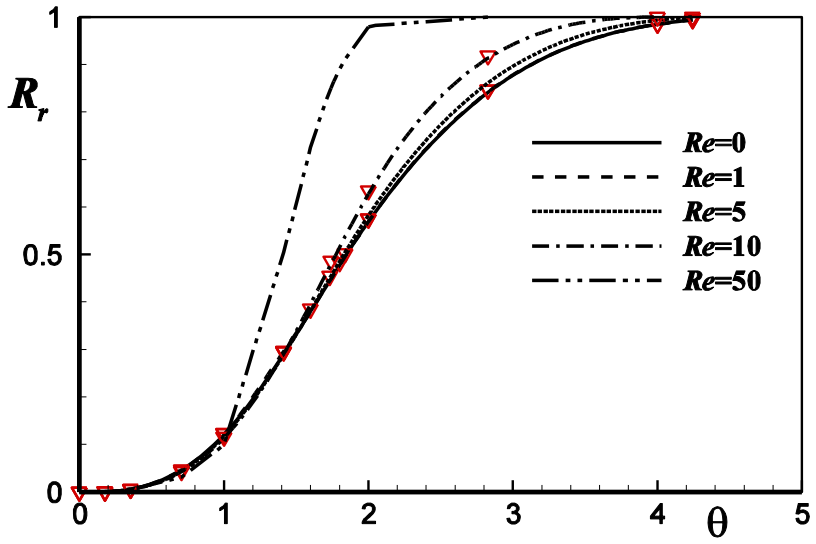

Figure 5: Degree of reverse to unidirectional flow for several gap widths, θ, and Reynolds numbers, for the Newtonian case. M25 (symbols) and M51 (lines).

In contrast to the subcritical condition, for a supercritical non-dimensional gap size ($\theta \geq 2$) viscoelasticity is now responsible for a continuous increase in R_r and the flow pattern here is similar to that of Figure 7 (b). It is important to note here that this supercritical pattern has not yet been observed experimentally because of the stabilising effect of inertia that will be discussed later.

For inertialess flow and intermediate gap widths ($1.7 \leq \theta \leq 2$, cf. Figure 6 for $\theta = 1.74$) a steady bi-stable bifurcation flow pattern is observed, with a sudden jump between the two flow configurations at slightly different Deborah numbers. The corresponding streamline plots are shown in Figure 7 for $De = 0.351$ and $\theta = 1.74$. On the upper plot the flow is quasi unidirectional ($R_r = 0.047$) and at the bottom plot the flow is highly reversed ($R_r = 0.85$). The bifurcation between these two flow patterns is due to a purely-elastic instability since $Re = 0$, as also observed for a

cross-slot geometry [9]. Incidentally, for $\theta = 1.74$ we find $R_r = 0.5$ and this corresponds to the situation where for a Newtonian fluid the approach flows at the stagnation point were closer to perpendicular. Here, the critical Deborah number is 0.316, a value close to that reported for the cross-slot geometry instability ($De_{crit} \approx 0.31$ [9]). The predictions also showed that in this intermediate region the critical *De* decreases in inverse proportion to θ. Regarding the effect of flow inertia, the critical *De* for a bi-stable bifurcation increases with *Re*, as shown in Figure 8 for $\theta = 1.74$ and $Re = 1$.

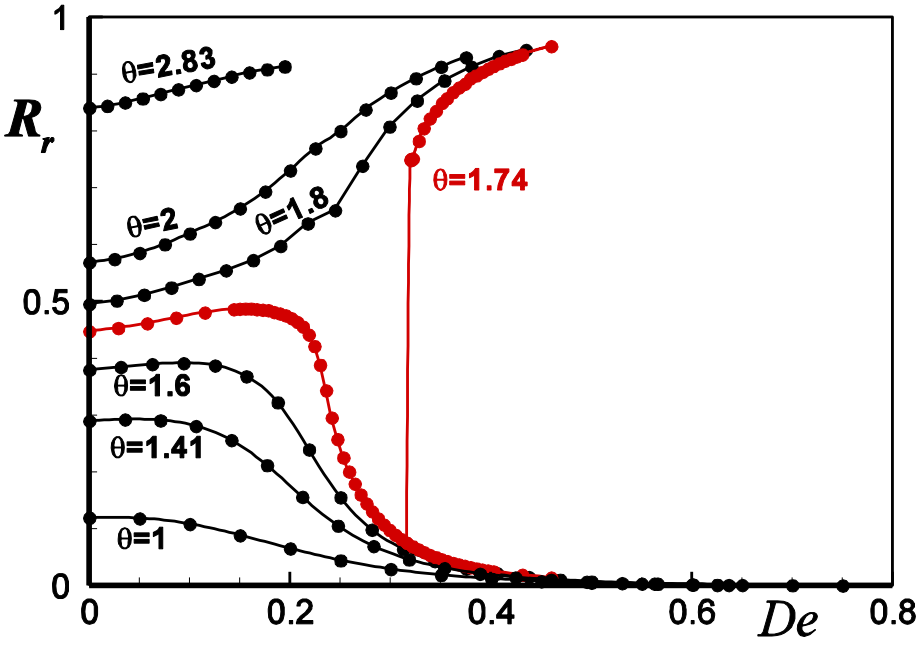

Figure 6: Degree of reverse to unidirectional flow for several gap widths, θ, and Deborah numbers, for *Re* = 0.

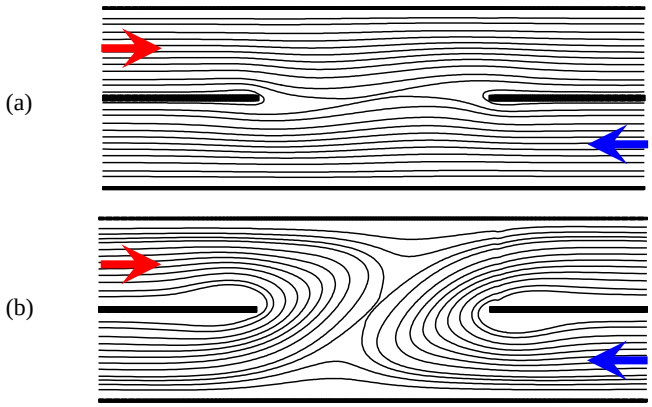

Figure 7: Streamlines for $\theta = 1.74$, with $\alpha = 0$, *Re* = 0 and *De* = 0.351 in mesh M51: the two bifurcated solutions have (a) $R_r = 0.047$ and (b) $R_r = 0.85$.

The combined effects of inertia and elasticity are illustrated in Figure 8, where R_r is plotted as a function of *De* for three different gap widths ($\theta = \sqrt{2}$, 1.74 and 2) and for *Re* up to 10. As for Newtonian fluids the degree of flow reversal is independent of Reynolds number for $Re \leq 1$. At higher Reynolds numbers (*Re* = 5 and 10) and $\theta = 2$ an inversion in the flow configurations is observed: whereas at low *Re* viscoelasticity was seen to be responsible for an increase in R_r, at large Reynolds numbers R_r decreases with *De* and becomes more unidirectional because the flow is subcritical. This is also in contrast with the Newtonian behavior where for the same value of $\theta = 2$ an increase in the Reynolds number increased the reversed flow. This opposed effect of inertia explains why the supercritical behavior has not yet been observed and suggests the need for further experiments, using a highly viscous and elastic fluid, to attain lower Reynolds numbers with high Deborah number flows.

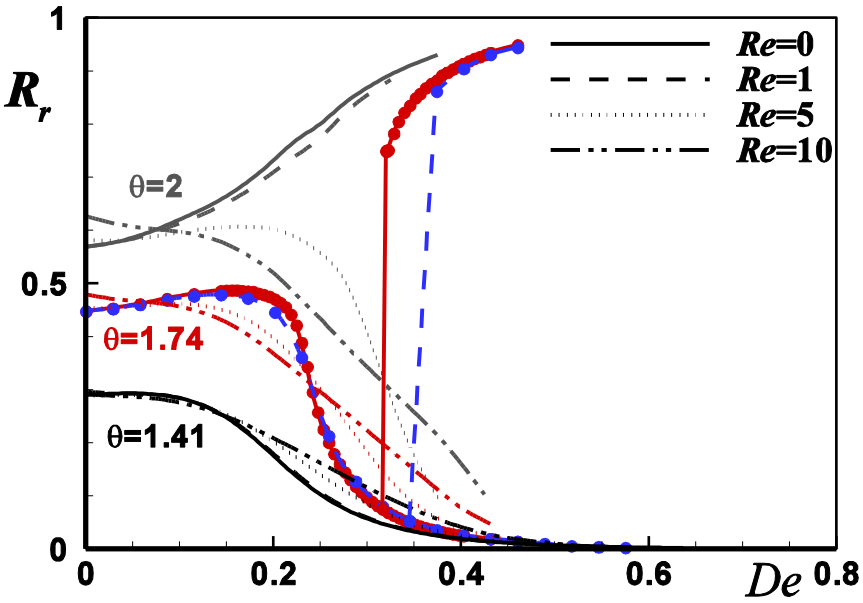

Figure 8: Degree of reverse to unidirectional flow for several gap widths, θ, and Deborah numbers, for *Re* = 0, 1, 5 and 10.

5 Conclusions

The UCM model was used to simulate viscoelastic flows in a mixing and separating geometry [1] and, for a combination of critical flow geometries, it was possible to identify a new steady bi-stable bifurcation pattern at low inertia and high elasticity.
The creeping flow of UCM fluids showed two distinct flow patterns. For normalized gap sizes below a critical value the reversed flow is slightly enhanced by viscoelasticity, followed by a strong decrease in R_r towards zero as *De* further increases. In contrast, above a supercritical gap size viscoelasticity is responsible for a continuous increase in R_r. For near-critical flow geometries it was possible to observe a sudden jump between the two flow conditions at slightly different Deborah numbers. Flow inertia was found to increase the critical Deborah number for steady flow bifurcation at a particular value of θ. Inertia naturally enhances the

straight flow case and at $Re = 5$, R_r always decreased with Deborah number for $De \leq 0.6$ and for the investigated gap sizes. These predictions suggest the need for experiments with very viscous elastic fluids (or at microscale where *Re* is naturally low and *De* enhanced) in order to detect the supercritical behavior, which has so far not been reported in the literature.

Acknowledgements

The authors acknowledge the financial support from FEDER and FCT through projects PPCDT/EME/59338/2004, POCI/EQU/56342/2004, PTDC/EQU-FTT/ 71800/2006 and scholarship SFRH/BD/28828/2006 (A. Afonso).

References

[1] T. Cochrane, K. Walters and M.F. Webster, On Newtonian and non-Newtonian flow in complex geometries, Philos. Trans. R. Soc. London, A301 (1981) 163-181.

[2] K. Walters and M.F. Webster, On dominating elasto-viscous response in some complex flows, Philos. Trans. R. Soc. London, A308 (1982) 199-218.

[3] A. Baloch, P. Townsend and M.F. Webster, On the simulation of highly elastic complex flows. J. Non-Newt. Fluid Mech., 59 (1995) 111-128

[4] N. Fiétier, Numerical simulations of viscoelastic fluid flows by spectral element methods and time-dependent algorithm. PhD Thesis, Lausanne, EPFL (2002).

[5] D.V. Boger, Highly elastic constant-viscosity fluid. J. Non-Newt. Fluid Mech., 3 (1977) 87-91.

[6] N. Phan-Thien and R.I. Tanner, New constitutive equation derived from network theory. J. Non-Newt. Fluid Mech. 2 (1977) 353-365.

[7] R.B. Bird, P.J. Dotson and N.L. Johnson, Polymer solution rheology based on a finitely extensible bead-spring chain model. J. Non-Newt. Fluid Mech., 7 (1980), 213 - 235.

[8] P.E. Arratia, C.C. Thomas, J.D. Diorio and J.P. Gollub, Elastic instabilities of polymer solutions in cross-channel flow. Phys. Rev. Lett. 96 (2006)144502.

[9] R.J. Poole, M.A. Alves and P.J. Oliveira. Purely elastic flow asymmetries. Phys. Rev. Lett. 99 (2007) 164503.

[10] R.J. Poole, M.A. Alves, A. Afonso, F.T. Pinho and P.J. Oliveira, Purely elastic instabilities in a cross-slot flow. The SoR 79th annual meeting, Salt Lake City, USA (2007).

[11] A. Chow, A. Keller, A.J. Müller and J.A. Odell. Entanglements in polymer solutions under elongational flow: a combined study of chain stretching, flow velocimetry and elongational viscosity. Macromolecules, 21 (1988) 250-256.

[12] P.J. Oliveira, F.T. Pinho and G.A. Pinto, Numerical simulation of non-linear elastic flows with a general collocated finite-volume method. J. Non-Newt. Fluid Mech. 79 (1998) 1-43.

[13] M.A. Alves, P.J. Oliveira and F.T. Pinho, A convergent and universally bounded interpolation scheme for the treatment of advection, Int. J. Num. Meth. Fluids, 41 (2003) 47-75.
[14] J.P. van Doormal and G. D. Raithby, Enhancements of the SIMPLE method for predicting incompressible fluid flows, Numer. Heat Transfer, 7 (1984) 147-163.